Investigation of Turbulence Characteristics in a Gas Cyclone by Stereoscopic PIV

Zhengliang Liu, Jinyu Jiao, Ying Zheng, and Qikai Zhang
Dept. of Chemical Engineering, University of New Brunswick, 15 Dineen Drive, P.O. Box 4400, Fredericton, NB, Canada E3B 5A3

Lufei Jia
CANMET Energy Technology Center, 1 Haanel Drive, Ottawa, ON, Canada K1A 1M1

DOI 10.1002/aic.11013
Published online November 6, 2006 in Wiley InterScience (www.interscience.wiley.com).

Stereoscopic particle image velocimetry (Stereo-PIV) was used as the tool to observe the turbulence characteristics in a gas cyclone. In the cylindrical and conical parts of the cyclone, intensive fluctuation occurs in the inner quasi-forced vortex, especially in its core where the precessing vortex core dominates. In the dust hopper, strong turbulence is observed at the interface between the downward flow and the upward flow, as well as in the centerline of the cyclone. Turbulence intensity in the tangential, axial, and radial directions and the Reynolds stresses are seen to be anisotropic: this anisotropy provides the evidence of more appropriateness of the Reynolds stress model (RSM) than the standard k-ε model, and the renormalization-group k-ε model for numerical simulations in gas cyclones. Due to flow instability and back-mixing caused by the turbulence, separated particles could disperse into and be re-entrained by the upward flow from the bin to degrade the separation efficiency of the cyclone. © 2006 American Institute of Chemical Engineers *AIChE J,* 52: 4150–4160, 2006
Keywords: stereoscopic particle image velocimetry, turbulence, separation techniques, hydrodynamics, gas cyclones

Introduction

As a low-cost unit operation for the removal of solids from gases, gas cyclone separators are widely used in the petrochemical and process industries to separate dust from gas streams or for product recovery. The simplicity of construction and compactness, ease of maintenance, and flexibility with respect to high-temperature and pressure are some of the many advantages of cyclone separators compared to filters, scrubbers, and settlers in industrial dedusting. However, the swirling turbulent flow field inside cyclones is extremely complicated despite their simple geometry. Extensive research has been carried out, by both experimental investigation and numerical simulations,[1–6] to study the flow structure. The main purpose of the study has always been focused on improving the performance of cyclones, such as how to reduce the operating pressure drop to save energy and how to improve their separation efficiency for smaller particles.

Besides velocity information, flow properties, such as vorticity, strain-rate, Reynolds stress, and turbulence intensity are also very important to understand the fluid dynamics in the cyclone. Vorticity reflects the local rotation of the fluid, and its magnitude is proportional to the strength of the rotation. Reynolds stress acts as a measure of the influence of

Correspondence concerning this article should be addressed to Y. Zheng at yzheng@unb.ca.

turbulence on the mean steady flow. It is more important than the viscosity in turbulent flows. In numerical simulations, the anisotropy of Reynolds stresses is a criterion to select different turbulence models. All these properties are closely connected with energy and very useful when studying power consumption in cyclones. In addition, turbulence intensity also reflects the flow stability in cyclones, which has a significant effect on their separation performance. Fortunately, if accurate whole-field velocity fields are available, all the aforementioned flow properties can be obtained.

In this work, the three-dimensional (3-D) gas velocity fields in a gas cyclone have been measured with a novel nonintrusive visualization experimental technique: stereoscopic-particle image velocimetry (Stereo-PIV). The aforementioned flow properties, such as vorticity, strain-rate, Reynolds stresses, and turbulence intensity distribution are investigated from the instantaneous and time-averaged whole-field velocity fields obtained by Stereo-PIV. The appropriateness of different turbulence models for simulating the flow fields in gas cyclones is validated through the available distribution of Reynolds stresses. An understanding of the highly turbulent and nonstationary features of swirling motions inside gas cyclones will shed a light on how to advance their operating performance.

Experimental Setup

The experimental apparatus is depicted in Figure 1. The air stream was fed into the cyclone through a regenerative blower (Gast R6150J-2) with airflow capacity of 365 m^3/h. The pressure drop through the cyclone was determined by measuring the pressure difference between its inlet and outlet with a U-tube manometer. The inlet airflow rate being measured by a digital Pitot tube (Kimo AMI KS300) was controlled by a throttle valve and a bypass valve. Tiny sugar particles were added as tracer particles. A laser beam traveled through a set of lenses and changed into a thin light-sheet to illuminate the measured flow field. The images of the tracer particles, carrying the flow information of the field, were recorded by two CCD cameras and transferred to the computer for analysis.

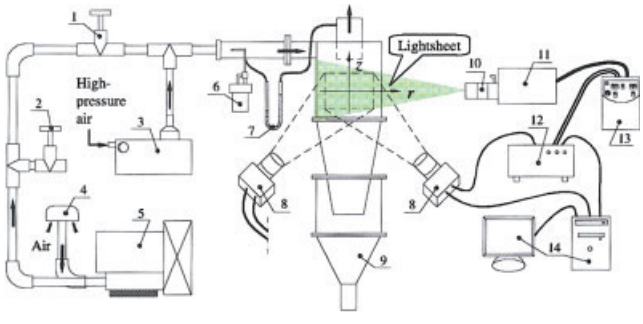

Figure 1. Experimental apparatus and PIV system.

[Color figure can be viewed in the online issue, which is available at www.interscience.wiley.com.]

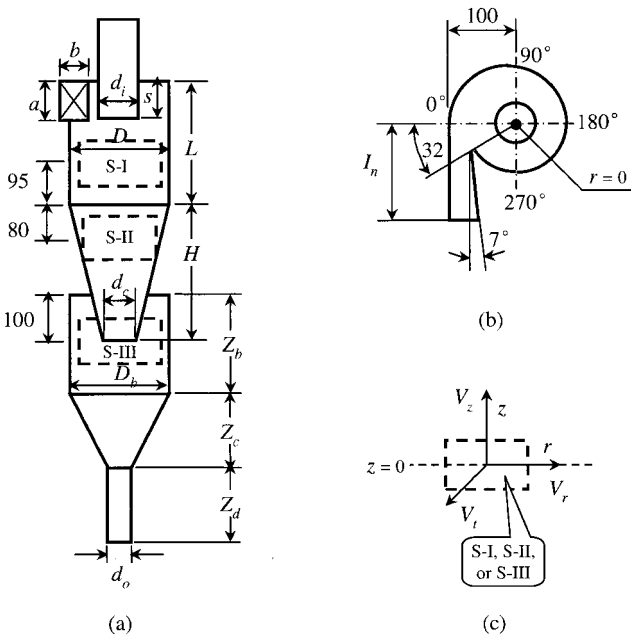

Figure 2. (a) Cyclone geometry, (b) the angular positions, and (c) the coordinate system used in the observing fields.

Cyclone geometry

The cyclone investigated in this study is made of Plexiglass with a volute inlet, as shown in Figure 2. All dimensions (units in mm) of the cyclone are listed in Table 1 in detail. Measurements were performed along two orthogonal (across 0°–180 and 90°–270°) axial sections in the cylindrical body, conical body, and dust hopper. The angular positions of the orthogonal axial sections are indicated in the top view in Figure 2b. The section of 0° – 180° is perpendicular to the volute inlet of the cyclone. S-I, S-II, and S-III refer to the observing fields in the cylindrical section, conical section, and dust hopper, respectively, and their sizes are given in Table 1. Their positions are shown in Figure 2 (a) where the numbers (95, 80, and 100 mm) indicate the distance between the horizontal center of the fields and their corresponding reference surfaces. The adopted coordinate system is shown in Figure 2c, in which the origin point sits at the geometrical center of the observing fields of S-I, S-II, and S-III.

A Reynolds number, *Re*, as well as a geometric swirl parameter, *S*, usually characterizes the swirling flow in a cyclone. Both parameters can be expressed in terms of geometrical factors and inlet conditions[7]

$$Re = \frac{\rho_f U_{in} b}{\mu_f}, \tag{1}$$

Table 1. Dimensions (mm) of the cyclone

a	b	d_c	d_i	d_o	D	D_b	I_n	L
68	46	60	65	30	150	150	150	260
H	s	Z_b	Z_c	Z_d	S-I	S-II	S-III	
330	68	200	150	100	140 × 105	120 × 90	140 × 105	

Table 2. Operating Conditions of the Experiments

Inlet Air Temperature(°C)	Inlet Air Velocity (m/s)	Inlet *Re* ($\times 10^4$)	Pressure Drop Through the Cyclone (pa)
40	7.2	2.0	274.5
	9.5	2.6	568.6
	12.2	3.4	980.3
	15.0	4.2	1519.5

$$S = \frac{\pi d_i D}{4ab}. \tag{2}$$

The swirl number for this cyclone is 2.45. The cyclone was operated at Reynolds number of $2.0 \times 10^4 \sim 4.2 \times 10^4$ with inlet air velocity varying from 7.2–15.0 m/s. Detailed operating conditions are listed in Table 2.

Seeding

Tiny sugar particles (density: 1.58×10^3 kg/m^3, refractive index: 1.54) were generated in a six-jet atomizer (TSI 9306A) by atomizing a 5 wt % sugar solution. The mean size of the sugar particles was around 0.8 micron in dia. Particle-number concentration was controlled by the number of jets in operation and the input pressure. Seeding in a strong swirling flow, such as that found in cyclones, is critical to experiments. First, the tracer particles are required to follow the centrifugal airflow strictly. To determine the ability of tracer particles to follow the fluid and the speed at which the seed particles respond to the flow changes, the particle Stokes number (*St*) is usually introduced. It is defined as

$$St = \tau_p/\tau_f, \tag{3}$$

where τ_p is the characteristic time of tracer particles or velocity response time, and τ_f is the characteristic time of the vortex field

$$\tau_p = (2\rho_p + \rho_f) \cdot d_p^2/36\mu_f \approx \rho_p \cdot d_p^2/18\mu_f \text{ (for } \rho_f \ll \rho_p), \tag{4}$$

$$\tau_f = R/V_t = D/2V_t. \tag{5}$$

When $St < 0.1$, the particle gravity is negligible, and the particle motion is considered as representing the fluid behavior.[8] In our experiments, the maximum Stokes number was less than 0.001, which indicates that the seeding particles can follow the gas motion without slip.

Another consideration is whether the presence of seeding particles will modulate the gas-phase behavior. In case of higher-mass loading, the turbulence of the gas phase will be modulated by the presence of seeding particles. According to Elgobashi,[9] the particle volume fraction and the density ratio (ρ_f/ρ_p) determine the relative significance of the influence of particles. When $\rho_f/\rho_p \approx 10^{-3}$, and the particle volume fraction is less than 10^{-6}, the influence of small particles on turbulence is negligible. This is the case in this study, so the turbulence intensity of the gas phase will not be modulated by the seeding particles.

PIV system

The PIV system includes an image capture component (two CCD cameras and two frame grabbers), an illumination component (the laser generator and lightsheet optics), a synchronizer, and an analysis component (the computer hardware and software).A thin vertical lightsheet with a wavelength of 532 nm is generated by a double-pulsed Nd:YAG laser (New Wave Research Solo III-15) through a set of cylindrical and spherical lenses. The lightsheet illuminates the gas flow in different parts of the cyclone where the investigation is focused. The laser pulse duration is 6 ns with energy of 50 mJ per pulse and repetition rate of 10 Hz. The frame straddling technique is applied to measure the flow filed. Two successive exposures of tracer particles to the laser lightsheet were recorded in two separate frames by both high-resolution (1600 $\times$ 1200 pixel) CCD cameras (TSI, model 630151) that were arranged with Scheimpflüg stereoscopic configuration. The time interval between the successive exposures was set to 20 – 50 microseconds depending on the values of the inlet gas velocity of the cyclone. The rule of thumb is that the particle image displacements are typically less than 1/4 of the interrogation window during the time interval. Two frame grabbers in the computer (Dell workstation, CPU 2.20 GHz) read the camera images and passed the information to the computer system for processing. The cameras recorded five pairs of frames per second. Dividing the particle images into smaller interrogation windows, a pair of 2-D velocity vector fields was first calculated by cross-correlation method, and then combined to a 3-D vector field where the tangential, axial, and radial velocities were obtained simultaneously. The size of the interrogation areas was 32 $\times$ 32 pixels, giving a spatial resolution of 2.1 mm in the conical section and 2.5 mm in the cylindrical section and dust hopper. The instantaneous three-dimensional velocity fields were obtained at a rate of five fields per second. All the data analysis was completed by a commercial software Insight 5.0 provided by TSI. For details of the principle of Stereo-PIV, the Scheimpflüg configuration of cameras, and perspective calibration, refer to Liu et al.[10]

Turbulence Models

Turbulent flow of gas cyclones is characterized by fluctuating velocity fields. It is unlikely to have a complete time-dependent solution of the exact Navier-Stokes equations. Reynolds averaging is an alternative approach in practical engineering calculations. The Reynolds-averaged Navier-Stokes (RANS) equations are written as

$$\frac{\partial \rho}{\partial t} + \frac{\partial(\rho u_i)}{\partial x_i} = 0, \tag{6}$$

$$\frac{\partial(\rho u_i)}{\partial t} + \frac{\partial(\rho u_i u_j)}{\partial x_j} = -\frac{\partial p}{\partial x_i} + \frac{\partial}{\partial x_j}\left[\mu\left(\frac{\partial u_i}{\partial x_j} + \frac{\partial u_j}{\partial x_i} - \frac{2}{3}\delta_{ij}\frac{\partial u_t}{\partial x_t}\right)\right] + \frac{\partial(-\rho\overline{u_i' u_j'})}{\partial x_j}, \tag{7}$$

where $-\rho\overline{u_i' u_j'}$ is known as the Reynolds stress tensor, which represents the effects of turbulence. In order to close the RANS equations, the Reynolds stresses must be modeled. Three popular turbulence models are generally used to close these equations: the standard k-ε model, renormalization-group (RNG) k-ε model, and the Reynolds stress transport model (RSM).

In the standard and RNG k-ε models, the Boussinesq hypothesis is commonly employed to relate the Reynolds stresses to the mean-velocity gradients

$$-\rho\overline{u_i'u_j'} = \mu_t\left(\frac{\partial u_i}{\partial x_j}+\frac{\partial u_j}{\partial x_i}\right)-\frac{2}{3}\left(\rho k+\mu_t\frac{\partial u_i}{\partial x_i}\right)\delta_{ij} \qquad (8)$$

The advantage of this approach is its relatively low-computational cost; however, its disadvantage is the bold assumption of turbulent viscosity (μ) being an isotropic scalar quantity, which is not strictly true for swirling flows, as in gas cyclones.

By abandoning the isotropic turbulent viscosity hypothesis adopted by the standard and RNG k-ε models, the RSM closes Navier-Stokes equations by solving transport equations for each component of the Reynolds stresses. The transport equations of the Reynolds stresses can be written as[5]

$$\frac{\partial}{\partial t}(\rho\overline{u_i'u_j'})+\frac{\partial}{\partial x_k}(\rho u_k\overline{u_i'u_j'}) = D_{ij}+P_{ij}+\Pi_{ij}-\varepsilon_{ij} \qquad (9)$$

where D_{ij} the term is stress diffusion, where P_{ij} is stress production, where Π_{ij} is pressure-strain, and where ε_{ij} is turbulent dissipation. where P_{ij} does not require modeling, while D_{ij}, Π_{ij} and ε_{ij} need to be modeled to close the equations. For further modeling of them, refer to Hu et al.[5]

Results and Discussion

Velocity fields in the cyclone

The instantaneous and time-averaged whole-field gas velocities in the tangential, axial, and radial directions in the whole cyclone were recorded simultaneously with the stereoscopic PIV. For a clearer view, velocity profiles were extracted from the time-averaged whole-field velocity fields, as shown in Figure 3. It shows the profiles of the tangential and axial velocities at three axial positions ($z = -30$ mm, 0, 30 mm) in both of the cylindrical (S-I), and conical (S-II) sections of the cyclone. The profiles of tangential velocities are antisymmetrical and slightly off-centered. They are nearly independent of the axial locations. They show a typical feature of a strong swirling flow with the existence of the Rankine-vortex structure, which includes the inner quasi-forced vortex and outer quasi-free vortex. The interface between the inner and outer vortexes, where tangential velocities reach the maximum, occurs at the position of $r = 26$ mm ($|r/R| = 0.35$), and is basically independent of the axial locations. The profiles of the axial velocities, which show a nonideal symmetry, have a two-peak shape consisting of an inner upward-flow zone and an outer downward-flow zone near the cyclone wall where the separated particles are transported downward.

Figure 4 shows two instantaneous axial velocity fields, which vary with time, in the cylindrical section. The time-averaged profiles in Figure 3 indicate an upward flow (positive values) in the inner core region of the cyclone. However, it is seen that a reverse flow occurs and moves in the inner core of the quasi-forced vortex around the cyclone axis, as shown in Figures 4a and b. This reversal is generated by the motion of precessing vortex core (PVC), which is usually associated with vortex breakdown, and the insurgence of reverse flow.

Figure 5 illustrates a typical time-averaged velocity vector field in the dust hopper (S-III), where the white-striped areas

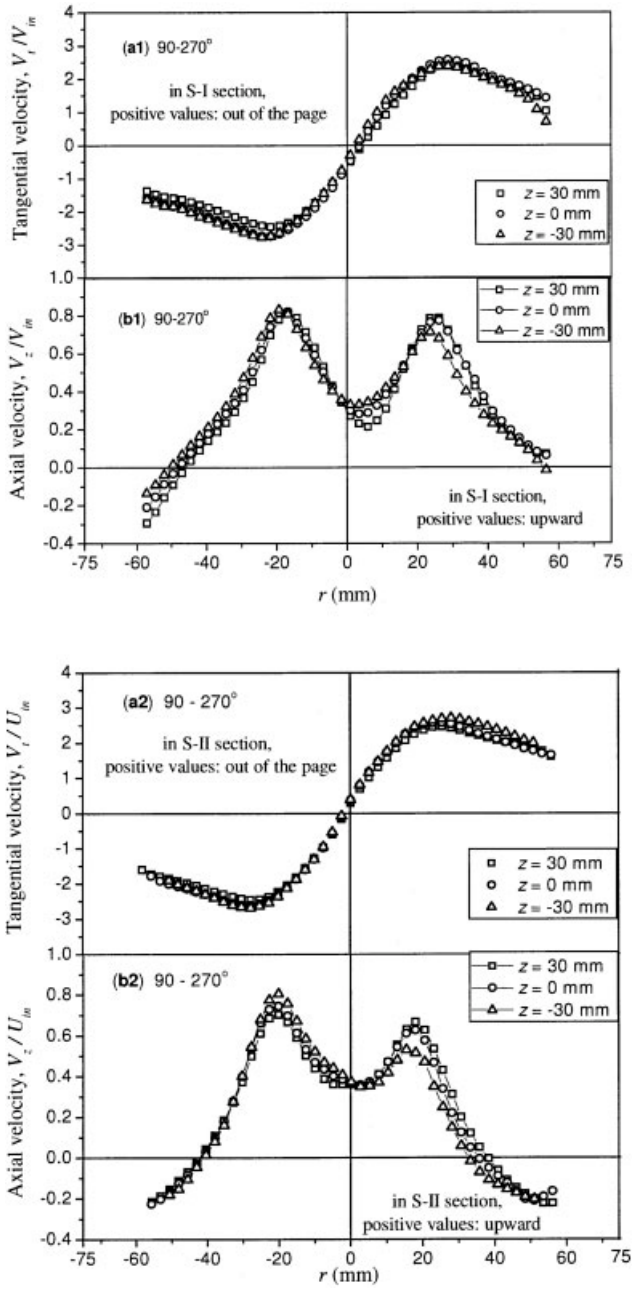

Figure 3. Typical time-averaged velocity profiles of (a1) tangential velocity and (b1) axial velocity in the cylindrical body (S-I), and profiles of (a2) tangential velocity, and (b2) axial velocity in the conical body (S-II).

enclosed by dash-dot lines mark off the wall of the conical body extruding into the bin and its surrounding area. It is clearly seen that a secondary longitudinal circular flow is formed in the annulus area of the dust hopper. Some of the separated particles will be circulated in the secondary flow, and make collecting them difficult in the bin. At the bottom of the conical body, a small amount of the secondary flow is entrapped in the upward flow, causing so-called "back-mixing". Due to back-mixing, separated particles could be captured by the upward flow, and be entrained out of the cyclone.

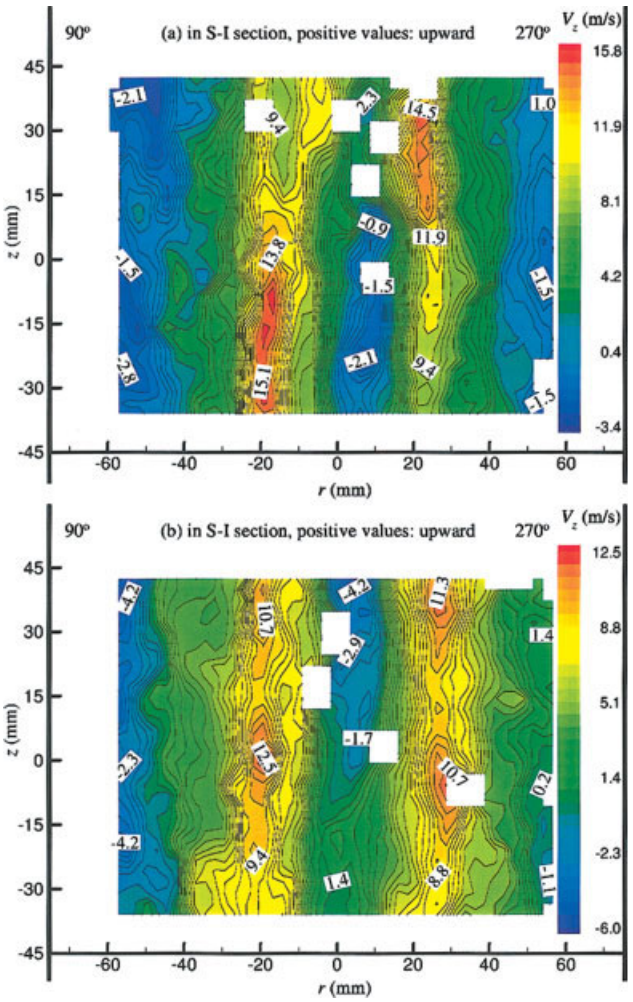

Figure 4. Instantaneous axial velocity fields at (a) time t_1, and (b) time t_2 in the cylindrical body (S-I).

[Color figure can be viewed in the online issue, which is available at www.interscience.wiley.com.]

Vorticity and strain-rate in the cyclone

Vorticity is a vector that moves in a way that mirrors the motion of the fluid itself. If the fluid is stretched, vorticity will increase along the axis of stretching. From the 3-D velocity fields detected by Stereo-PIV, the tangential components of the vorticity and strain-rate are obtained. Unfortunately, the axial and radial components are not available. The vorticity in the tangential direction is defined by

$$\omega_t = \frac{\partial V_z}{\partial r} - \frac{\partial V_r}{\partial z}. \tag{10}$$

The strain-rate here refers to the shear rate of strain or the shear angular velocity. It is also a vector, and its value in the observed plane is given by

$$\xi_t = \frac{1}{2}\left(\frac{\partial V_z}{\partial r} + \frac{\partial V_r}{\partial z}\right). \tag{11}$$

Similar to the behavior of the instantaneous velocity fields, the instantaneous vorticity and strain-rate fields fluctuate from time to time. The typical ones in the cylindrical body are shown in Figure 6 where they are normalized by dividing the inlet gas velocity (U_{in}). The striking feature is that the vorticity and the strain-rate vary randomly in the whole field and contain irregular patterns. However, if they are calculated based on the time-averaged velocity fields, regular patterns are obtained, as shown in Figure 7. It is interesting to note that the vorticity and strain-rate have very similar distribution patterns despite different magnitudes. In addition, similar distributions are obtained across both axial sections despite different inlet gas velocities. Figure 7 shows relatively weak vorticity and strain-rate near the wall. Around the positions corresponding to the peak and trough in the two-peak distribution of axial velocity (Figure 3), their values are near zero. In contrast, strong vorticity and strain-rate exist along both sides of the peak of the axial velocity. Similar vorticity and strain-rate distributions, which are not shown here, are also observed in the conical body.

In the dust hopper, as shown in Figure 5, the outer vortex expands outwards and downward due to disappearance of the constraint of the conical body. As a result, a secondary eddy, showing strong vorticity in Figure 8, is formed at the outer edge of the expanding downward flow. At the same time, another secondary eddy is generated where the inner upward flow encounters the outer downward flow. As a result, a pair of counter-rotating vortices exists at both sides of the downward flow. By comparing Figure 8 to Figure 7, it is clearly seen that the magnitude of the vorticity in the counter-rotating vortices in the dust hopper is much higher than that in the cylindrical and conical sections. For example, the magnitude of the strongest vorticity in the cylindrical section is 50 times that of the gas inlet velocity, whereas it can reach over 100 times that of the gas inlet velocity in the counter-rotating vortices.

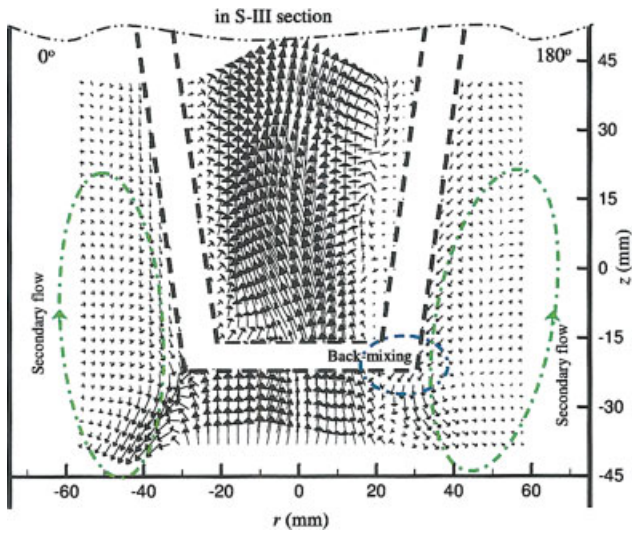

Figure 5. A typical time-averaged velocity vector field in the dust hopper.

[Color figure can be viewed in the online issue, which is available at www.interscience.wiley.com.]

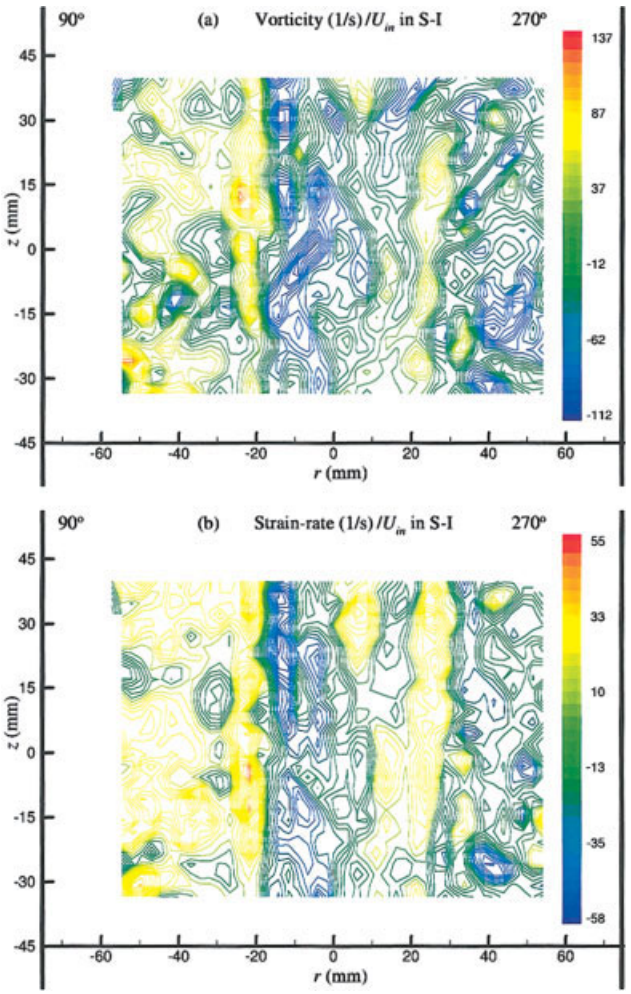

Figure 6. Instantaneous (a) vorticity field, and (b) strain-rate field in the cylindrical body (S-I).

[Color figure can be viewed in the online issue, which is available at www.interscience.wiley.com.]

Reynolds stresses in the cyclone

Reynolds stress is a tensor with three normal components, and three pairs of shear components. Each pair is assumed to be equal, so there are actually six values. Divided by gas density, its normal and shear components are

$$-\overline{(V_i')^2} = \frac{1}{N}\sum_{n=1}^{N}(V_i^{t_n} - \overline{V_i})^2; \tag{12}$$

$$-\overline{V_r'V_z'} = \frac{1}{N}\sum_{n=1}^{N}[(V_r^{t_n} - \overline{V_r}) \cdot (V_z^{t_n} - \overline{V_z})]; \tag{13}$$

$$-\overline{V_z'V_t'} = \frac{1}{N}\sum_{n=1}^{N}[(V_z^{t_n} - \overline{V_z}) \cdot (V_t^{t_n} - \overline{V_t})]; \tag{14}$$

$$-\overline{V_r'V_t'} = \frac{1}{N}\sum_{n=1}^{N}[(V_r^{t_n} - \overline{V_r}) \cdot (V_t^{t_n} - \overline{V_t})]; \tag{15}$$

where $i = t$, z, and r, representing the tangential, axial, and radial directions, respectively; N is the total number of instantaneous velocity at a specified location; and t_n is the time series.

Figure 9a, b, and c illustrate typical contours of the three shear components of the Reynolds stress in the cylindrical body of the cyclone. They are normalized by divided by the inlet gas velocity square (U_{in}^2). Figure 9 shows that the Reynolds stresses are generated inhomogeneously across the section. Higher Reynolds stresses are usually produced in the center while much lower values are produced in the outer region. To investigate the anisotropy of the Reynolds stresses, each component of the Reynolds stresses at specified locations should be compared. By extracting from Figure 9a, b, and c, the profiles of each shear component are compared in Figure 9 d1 and d2 at two axial positions. The divergent profiles at both axial positions show that the Reynolds stresses are anisotropic across the section. On the other hand, the anisotropy is much weaker in the outer region of the cyclone.

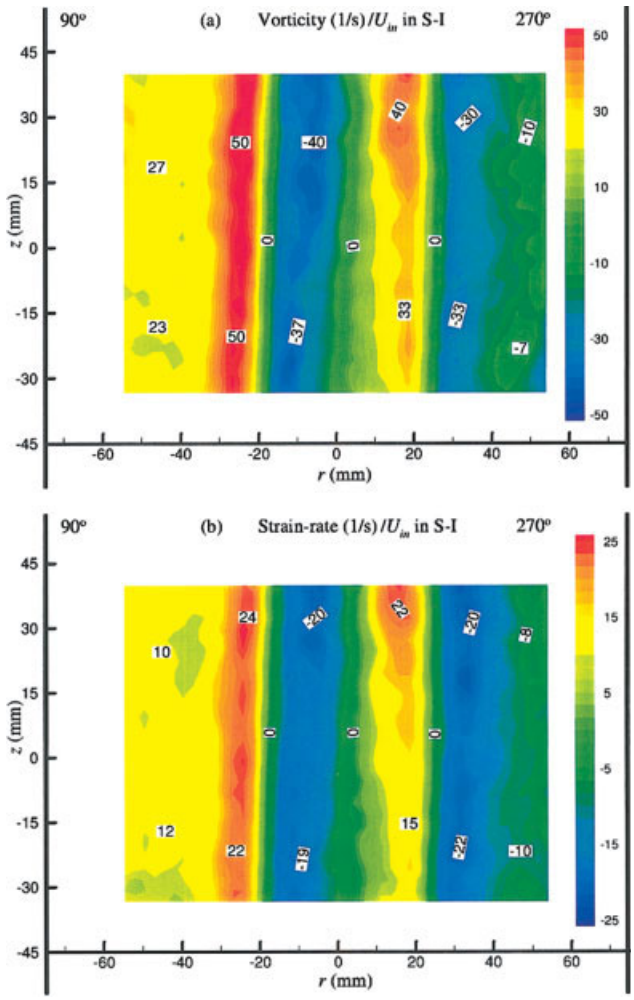

Figure 7. Distribution of (a) vorticity, and (b) strain-rate in the time-averaged velocity field in the cylindrical body (S-I).

[Color figure can be viewed in the online issue, which is available at www.interscience.wiley.com.]

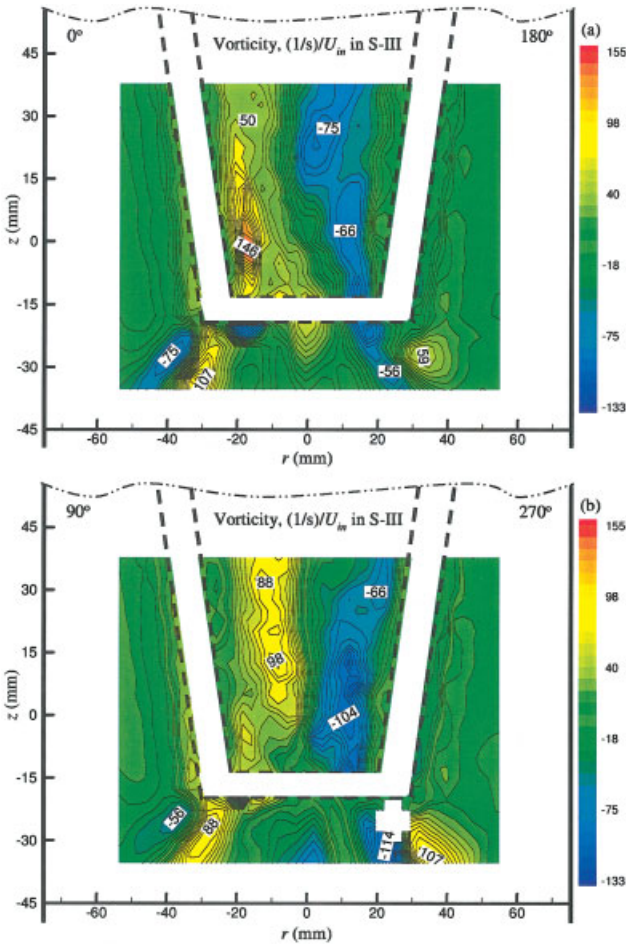

Figure 8. Typical distribution of vorticity in the time-averaged velocity field across both (a) 0-180° and (b) 90–270° sections in the dust hopper (S-III).

[Color figure can be viewed in the online issue, which is available at www.interscience.wiley.com.]

In numerical simulations, the standard and RNG k-ε models adopt the isotropic turbulent viscosity hypothesis whereas the RSM model employs anisotropic turbulence. The presence of anisotropic Reynolds stresses in Figure 9 predicts that the RSM is more appropriate for such a swirling flow in gas cyclones in comparison with the other two models. This prediction is confirmed by the comparisons of the experimental data with the simulation results by different turbulence models, as depicted in Figure 10. It shows that the simulations of the tangential and axial velocity profiles by the RSM are more in agreement with the experimental data than the simulations by the standard and RNG k-ε models, despite the two-peak shape of the axial velocity not being well predicted. The simulation results also confirm what was reported by Hoekstra et al.[1], that the RSM performed better than the other two models. The obtained contours of Reynolds stresses in this study are possibly helpful to optimize the coefficients in the RSM to improve the simulation results. Recently, research on swirl combustors indicated that the

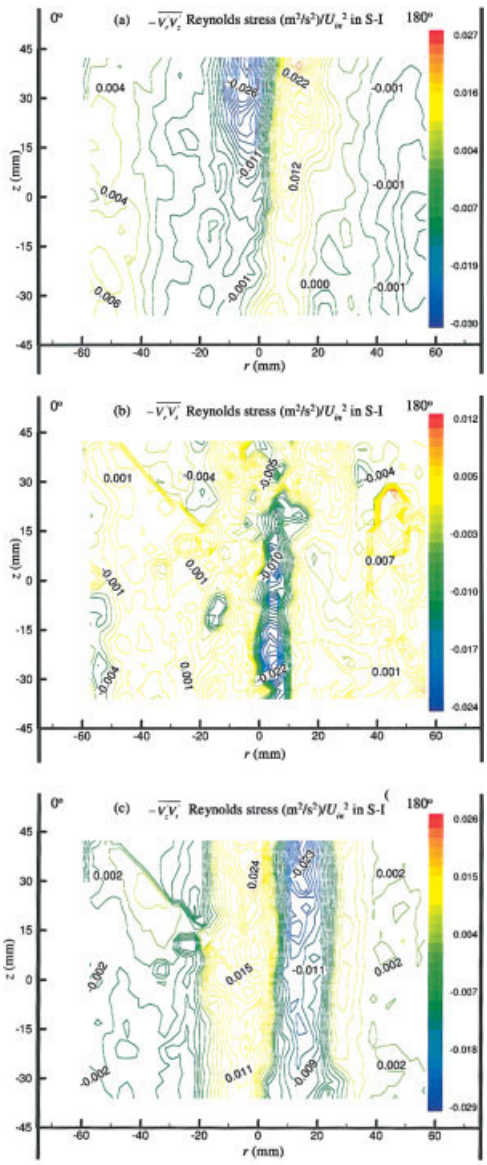

Figure 9. Contours of (a) $-\overline{V_r'V_z'}$, (b) $-\overline{V_r'V_t'}$, and (c) $-\overline{V_z'V_t'}$ Reynolds stresses across 0–180° section; and their profiles at (d1) z = 30 mm, and (d2) z = −30 mm in the cylindrical body (S-I).

[Color figure can be viewed in the online issue, which is available at www.interscience.wiley.com.]

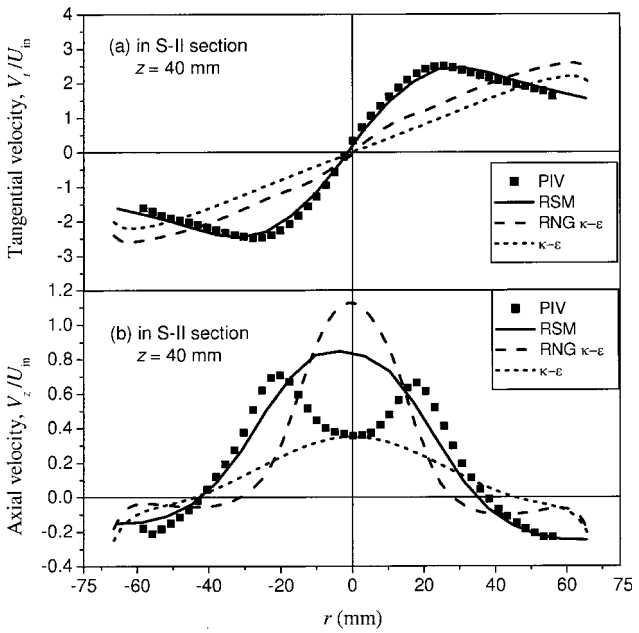

Figure 10. Comparisons between the experimental data and simulation results by different turbulence models.

large eddy simulation (LES) is a promising method for predicting the unsteady swirling flow.[11,12]

Turbulence in the cyclone

The turbulence intensity (E) is calculated from the root mean square of the turbulence fluctuation of the instantaneous liquid velocities, as defined by

$$E_i = \sqrt{\frac{1}{N}\sum_{n=1}^{N}(V_i')^2} = \sqrt{\frac{1}{N}\sum_{n=1}^{N}(V_i^{t_n} - \overline{V_i})^2}, \qquad (16)$$

where $i = t$, z, and r, representing the tangential, axial, and radial directions, respectively.

The total turbulence intensity is given by

$$E_{total} = \sqrt{\frac{1}{3}(E_t^2 + E_z^2 + E_r^2)}. \qquad (17)$$

To remove the effect of the inlet gas velocity, the turbulence intensity is also normalized. Figure 11a and b show the profiles of individual turbulence intensity in the radial, axial, and tangential directions in the cylindrical and conical bodies, respectively. Apparently, the profiles are divergent in different directions. As the discussion in the "*Reynolds stresses in the cyclone*" section about the Reynolds stresses, the divergence also indicates that the turbulence intensity is anisotropic. The anisotropy is strongest around the centerline of the cyclone. The anisotropy of the turbulence intensity also proves the appropriateness of the RSM for numerical simulations.

For the total turbulence intensity, its typical contours across both 0–180° and 90–270° axial sections in the cylindrical body are shown in Figure 12a and b, respectively. It is seen that the distributions across both sections are quite similar. Strong turbulence occurs inside the inner quasi-forced vortex, especially around the centerline of the cyclone where the precessing vortex core (PVC) prevails. The PVC, which exists in the center of cyclones and causes periodical gas velocity fluctuation, was observed by previous researchers.[1,13,14] It is interesting to note that a slightly wider area of strong turbulence occurs at the upper part of the cylindrical body that is close to the bottom of the vortex finder. This occurrence is not surprising because strong fluctuation is produced around the bottom of the gas outlet. When moving down along the axial direction, the influence of the vortex finder decreases. In the low-part of the cylindrical body, Figure 12 shows the total turbulence intensity having a typical three-zone distribution that is also presented in the conical body, as elucidated in the following discussion.

Typical profiles of the total turbulence intensity distribution in the lower part of the cylindrical body, and in the conical body are depicted in Figure 13. The profile (at $z = -30$ mm in S-I), representing the distribution in the lower part of cylindrical body is extracted from Figure 12 a. It is clearly seen that there are typical three zones (marked with numbers in Figure 13) in the distribution of the total turbulence. For the outer region ($0.35 < |r/R| < 1$) where the quasi-free vortex exists, the flow is less turbulent with almost a constant intensity. In the inner region ($0.1 < |r/R| < 0.35$) where the quasi-forced vortex exists without the influence of the PVC, the fluctuation keeps increasing along the inward radial direction to a moderate level. In the core of the inner vortex ($0 < |r/R| < 0.1$), where the PVC dominates, the produced turbulence jumps to a high level. From Figure 11a and b, it is clearly seen that this three-zone distribution is also the case for the individual turbulence intensity in the tangential, axial, and radial directions.

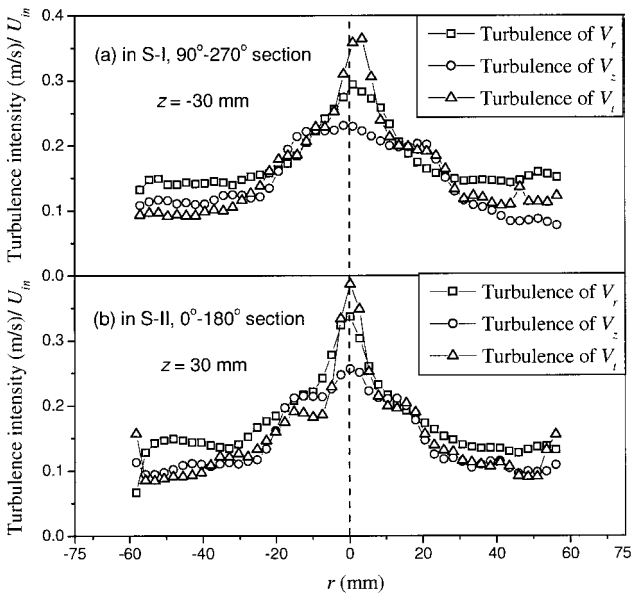

Figure 11. Profiles of the radial, axial, and tangential turbulence intensity in the cylindrical (S-I) and conical (S-II) bodies.

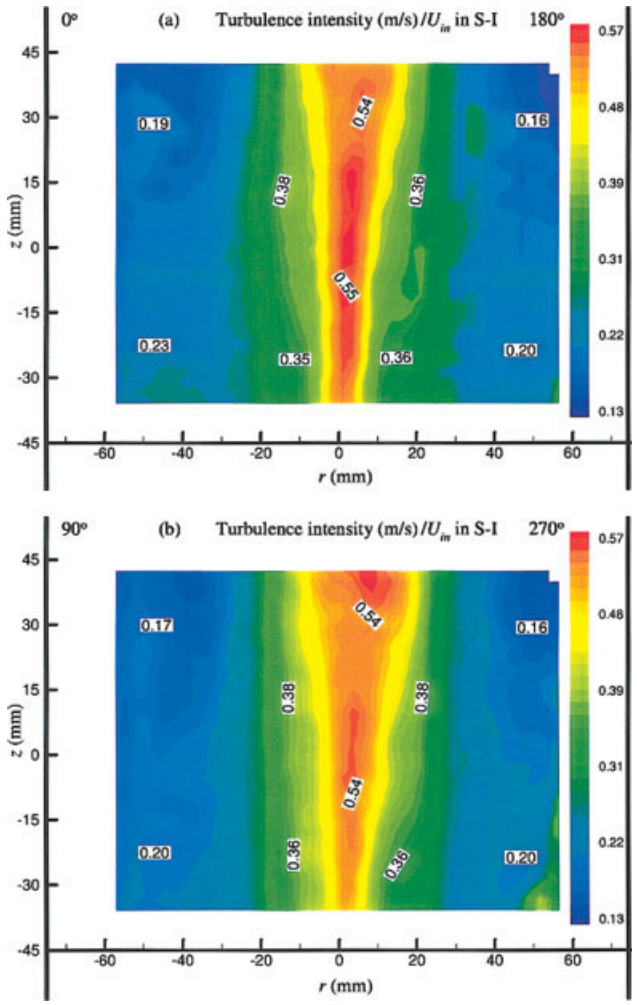

Figure 12. Typical distribution of total turbulence intensity across both (a) 0–180° and (b) 90–270° sections in the cylindrical body (S-I).

[Color figure can be viewed in the online issue, which is available at www.interscience.wiley.com.]

The maximum turbulence intensity occurring in the center of the cyclone was also observed by other researchers during experimental investigation and simulation.[1,5,5] They stated that most of the fluctuation was due to the precession of the vortex core, and the vortex core seemed to avoid the cyclone's center without a preferred angular position.[15] As indicated by the slightly off-centered velocity profiles in Figure 3, the rotation center of vortex precession does not always coincide with the geometrical center of the cyclone.

Figure 14 shows the instantaneously fluctuating tangential velocity in time series at different radial positions in each of the three zones ($z = 0$ is the same axial position as in Figure 13). The time interval is 200 ms, and the dash lines represent the averaged values. It is clearly seen that the tangential velocity fluctuates violently in zone three. Despite its average value of near zero, the instantaneous tangential velocity reaches as much as ± 8.0 m/s. The same fluctuating phenomena are also observed for the axial and radial velocities.

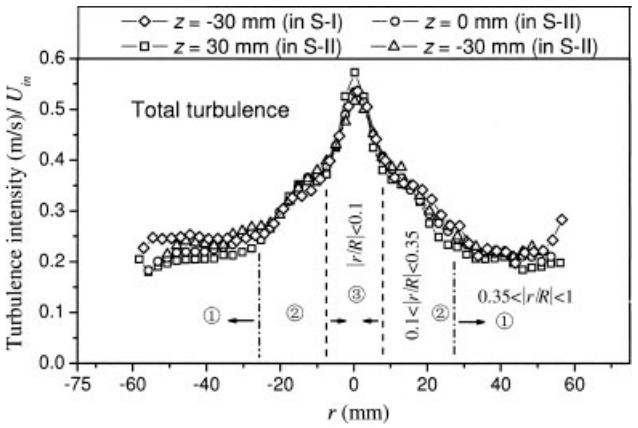

Figure 13. Profiles of the total turbulence-intensity distribution at lower-cylindrical body (S-I), and in the conical body (S-II).

In zone three, the fluctuation energy consists of two components: a random part and a periodic part

$$E = E_{random} + E_{pseudo}, \tag{18}$$

where E_{random} is the true turbulence and E_{pseudo} is the pseudo-turbulence caused by the periodic motion of the PVC. In zone one and two, E_{pseudo} equals zero. Consequently, the measured turbulent intensity by means of ensemble averaged root mean square (calculated by Eq. 16) in the core region of zone three is overestimated due to the existence of E_{pseudo}. The periodic oscillation contributor (E_{pseudo}) can be separated from chaotic turbulent fluctuations (E_{random}) on the required time and spatial resolutions.[16] Unfortunately, the sampling frequency of the PIV measurements in this

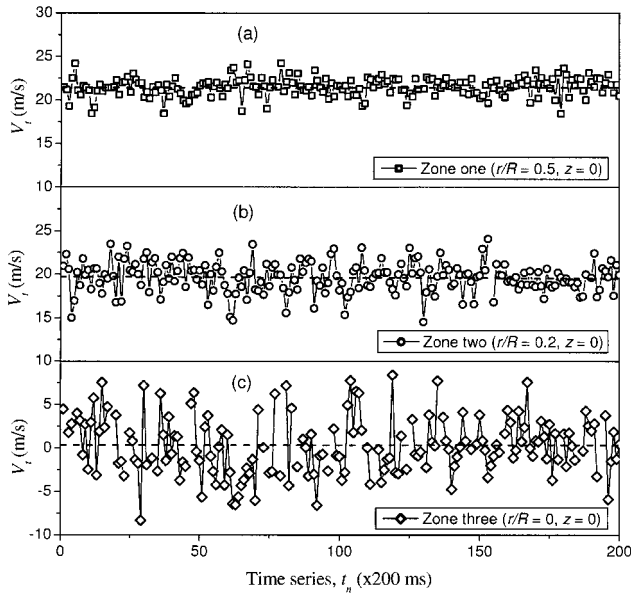

Figure 14. Instantaneous tangential velocity in different radial positions of (a) $r/R = 0$, (b) $r/R = 0.2$, and (c) $r/R = 0.5$ in the conical body (S-II) when $U_{in} = 12.2$ m/s.

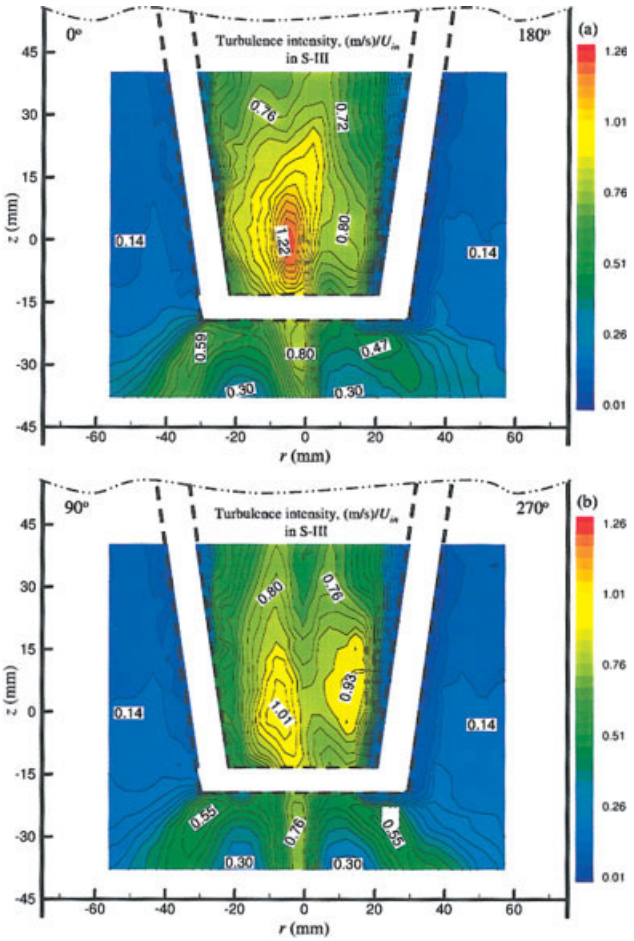

Figure 15. Typical distribution of total turbulence intensity across both (a) 0–180°, and (b) 90–270° sections in the dust hopper (S-III).

[Color figure can be viewed in the online issue, which is available at www.interscience.wiley.com.]

study is far below the frequency of periodic motion of the PVC in gas cyclones. As a result, the frequency of the PVC cannot be obtained and the pseudo-turbulence is usually hard to separate, although Graftieaux et al.[17] proposed a method of the proper orthogonal decomposition to separate it based on complex calculations. Recently, the need of phase locked PIV and laser Doppler anemometry (LDA) were suggested to use to separate the true turbulence from the fluctuation caused by the periodic motion of the PVC.[18]

Peng et al.[14] reported that the frequency of rotation of the PVC is proportional to the inlet gas flow rate, and our results show that the total fluctuation energy is also proportional to it. Turbulence cannot exist without a continuous supply of energy. The high turbulence caused by the PVC can produce possible work instability and negative effects on pressure drop across the cyclone, as shown in Table 2. When the gas inlet velocity doubled from 7.2 to 15.0 m/s, the pressure drop increased 5.5 times, despite some increase due to wall friction. Therefore, the hydrodynamics of the PVC is very important to understand and improve the performance of cyclones.

The turbulence intensity distribution stated above also sheds a light on the particle separation in the separation space of the cyclone. The flow of the inner quasi-forced vortex is much more unstable than that of the outer quasi-free vortex, especially in the core of the inner vortex. According to the "equilibrium orbit" theory, particles with different sizes have different equilibrium orbits where the centrifugal force is in balance with the drag force on them. Particles with equilibrium orbits beyond the separation surface will be separated. However, the strong flow instability of the inner vortex will break the equilibrium orbits and impose a negative effect on particle separation. Numerical simulation[19] showed that the separation efficiency decreases with increase in the turbulence intensity when the particles are less than 17.5 μm in diameter, but due to larger particles having higher inertias, its influence on the separation efficiency diminishes gradually as particle size increases. Similar results were also reported by Jiao et al.[20]

Figure 15 illustrates the turbulence distribution in the conical dust outlet and in the dust hopper. Very strong fluctuation is produced around the conical dust outlet. The fluctuation is even much higher than that in the separation space. Thus, back-mixing will be generated. Separated particles, which are already deposited on the wall, will be re-entrapped into the upward flow due to back-mixing. Unlike in the whole separation space where high-turbulence is produced only in the inner vortex core, in the dust hopper high-turbulence is also produced at the encountering interface between the downward flow and the upward flow. A very similar turbulence distribution pattern in the bin was reported by Obermair et al.[4] for their conventional cyclone of geometry A. The strong fluctuation and secondary eddy around the encountering interface will facilitate the back-mixing, as well as the dispersion of separated particles into the upward flow. Consequently, the separated particles could be recaptured by the upward flow, and entrained out of the gas outlet to degrade the separation efficiency of the cyclone.

Conclusions

The turbulence and other flow properties, such as vorticity, strain-rate, and Reynolds stresses of the 3-D strong swirling flow in a gas cyclone have been examined in this study. The anisotropy of turbulence intensity in the tangential, axial, and radial directions and the anisotropy of the Reynolds stresses in the gas cyclone provide the evidence that the Reynolds stress transport model (RSM) is more appropriate than the standard k-ε model and the renormalization-group k-ε model for numerical simulations in swirling flows. A typical three-zone distribution of the turbulence intensity is observed in the cylindrical separation space away from the influence of the vortex finder, and in the conical body. The fluctuation being produced in the inner quasi-forced vortex flow is much stronger than that in the outer quasi-free vortex flow, especially in the core of the inner vortex where the precessing vortex core dominates. The high-turbulence caused by the PVC may have a negative effect on the pressure drop and particle separation across the cyclone. Around the conical dust outlet, strong fluctuation will generate back-mixing to stir up the sedimentary particles from the wall. In the dust hopper, high-turbulence and secondary eddy being produced

around the encountering interface between the expanding downward flow and upward flow will facilitate the back-mixing and dispersion of particles. The separated particles could be re-entrained into the upward flow from the bin to degrade the separation efficiency of the cyclone.

Acknowledgments

The authors gratefully acknowledge the financial assistance from AIF, CFI, and NSERC.

Notation

a = cyclone inlet height, mm
b = cyclone inlet width, mm
d_c = cyclone conical body outlet diameter, mm
d_i = cyclone vortex finder diameter, mm
d_o = cyclone dust outlet diameter, mm
D = cyclone cylindrical body diameter, mm
D_b = cyclone dust hopper body diameter, mm
E = fluctuating energy, m/s
E_{random} = fluctuating energy caused by random turbulence, m/s
E_{pseudo} = fluctuating energy caused by pseudo-turbulence, m/s
I_n = cyclone inlet length, mm
k = turbulent kinetic energy, m^2/s^2
L = cyclone cylindrical body height, mm
N = number of instantaneous velocities
H = cyclone conical body height, mm
r = horizontal/radial coordinates
r_i = radius of cyclone vortex finder ($=d_i/2$), mm
Rt = radius of cyclone cylindrical body ($=D/2$), mm
Re = Reynolds number
s = extrusive vortex finder height, mm
S = geometric swirl number
St = Stokes number
t_n = time series
U_{in} = inlet air velocity, m/s
V = gas velocity in cyclone, m/s
z = vertical/axial coordinates
Z_b = cyclone cylindrical dust hopper height, mm
Z_c = cyclone conical dust hopper height, mm
Z_d = cyclone dust outlet height, mm

Greek letters

δ = Kronecker delta
μ = gas viscosity, Pa·s
μ_t = turbulent viscosity, Pa·s
ρ = gas density, kg/m^3
τ = characteristic time, s
ω = vorticity, 1/s
ξ = strain-rate, 1/s

Superscripts

$'$ = fluctuating component
$\overline{\ }$ = averaged

Subscripts

f = air phase
p = particle
r = radial coordinate
t = tangential coordinate
z = vertical/axial coordinate

Literature Cited

1. Hoekstra AJ, Derksen JJ, Van Den Akker HEA. An experimental and numerical study of turbulent swirling flow in gas cyclones. *Chem Eng Sci*. 1999;54:2055–2065.
2. Solero G, Coghe A. Experimental fluid dynamic characterization of a cyclone chamber. *Experimental Thermal and Fluid Sci*. 2002;27: 87–96.
3. Peng W, Hoffmann AC, Boot PJAJ, Udding A, Dries HWA, Ekker A, Kater J. Flow pattern in reverse-flow centrifugal separators. *Powder Technol*. 2002;127:212–222.
4. Obermair S, Woisetschläger J, Staudinger G. Investigation of the flow pattern in different dust outlet geometries of a gas cyclone by laser Doppler anemometry. *Powder Technol*. 2003;138:239–251.
5. Hu L-Y, Zhou L-X, Zhang J, Shi M-X. Studies on strongly swirling flows in the full space of a volute cyclone separator. *AIChE J*. 2005;51:740–749.
6. Griffiths WD, Boysan, F. Computational fluid dynamics (CFD) and empirical modeling of the performance of a number of cyclone samplers. *J of Aerosol Sci*. 1996;27:281–304.
7. Gupta AK, Lilley DG, Syred N. Swirling flows. Tunbridge Wills, UK: Abacus Press, 1984.
8. Brandon DJ, Aggarwal SK. A numerical investigation of particle deposition on a square cylinder placed in a channel flow. *Aerosol Sci and Technol*. 2001;34:340–352.
9. Elgobashi S. On predicting particle-laden turbulent flows. *Applied Scientific Research*. 1994;52:309–329.
10. Liu Z-L, Zheng Y, Jia L-F, Jiao J-Y, Zhang Q-K. Stereoscopic PIV studies on the swirling flow structure in a gas cyclone. *Chem Eng Sci*. 2006;61:4252–4261.
11. Selle L, Lartigue G, Poinsot T, Koch R, Schildmacher K-U, Krebs W, Prade B, Kaufmann P, Veynante D. Compressible large eddy simulation of turbulent combustion in complex geometry on unstructured meshes. *Combustion and Flame*. 2004;137:489–505.
12. Huang Y, Sung H-G, Hsieh S-Y, Yang V. Large-eddy simulation of combustion dynamics of lean-premixed swirl-stabilized combustor. *J of Propulsion and Power*. 2003;19:782–794.
13. Wu X-L, Shi M-X. Visualization of the precessing vortex core in a cyclone separator by PIV. *Chinese J of Chem Eng*. 2003;11:633–637.
14. Peng W, Hoffmann AC, Dries HWA, Regelink MA, Stein LE. Experimental study of the vortex end in centrifugal separators: The nature of the vortex end. *Chem Eng Sci*. 2005;60:6919–6928.
15. Derksen JJ, Van den Akker HEA. Simulation of vortex core precession in a reverse-flow cyclone. *AIChE J*. 2000;46:1317–1331.
16. Grosjean N, Graftieaux L, Michard M, Hübner W, Tropea C, Volkert J. Combining LDA and PIV for turbulence measurements in unsteady swirling flows. *Measurement Sci and Technol*. 1997;8: 1523–1532.
17. Graftieaux L, Michard M, Grosjean N. Combining PIV, POD and vortex identification algorithms for the study of unsteady turbulent swirling flows. *Measurement Sci and Technol*. 2001;12:1422–1429.
18. Syred N. A review of oscillation mechanisms and the role of the precessing vortex core (PVC) in swirl combustion systems. *Progress in Energy and Comb Sci*. 2006;32:93–161.
19. Li X-D, Yan J-H, Cao Y-C, Ni M-J, Cen K-F. Numerical simulation of the effects of turbulence intensity and boundary layer on separation efficiency in a cyclone separator. *Chem Eng J*. 2003;95:235–240.
20. Jiao J-Y, Zheng Y, Sun G-G. Numerical simulation of fine particle separation in a rotational tube separator. *China Particuology*. 2005; 3:219–223.

Manuscript received Mar. 7, 2006, and revision received Jun. 13, 2006, and final revision received Aug 25, 2006.